1 The impact of mineral reactive surface area variation on simulated mineral

2 reactions and reaction rates

- 3 Fanqi Qin, Lauren E. Beckingham*
- 4 Department of Civil and Environmental Engineering, Auburn University
- 5 *leb@auburn.edu

6 7

8

9

10

11

1213

14

15

16

17

18 19

20

2122

23

24

25

26

27

28

2930

31

32

Abstract

Reactive transport modeling is an essential tool to simulate complex geochemical reactions in porous media that can impact formation properties including porosity and permeability. However, simulating these reactions is challenging due to uncertainties in model parameters, particularly mineral surface areas. Imaging has emerged as a powerful means of estimating model parameters including porosity and mineral abundance, accessibility and accessible surface area. However, these parameters, particularly mineral accessible surface area, vary with image resolution. This work aims to enhance understanding of the impact of image resolution and other means of estimating mineral reactive surface area on simulated mineral reactions and reaction rates. Mineral surface areas calculated from images with resolutions of 0.34 µm and 5.71 µm were used to simulate mineral reactions in the context of geologic CO₂ sequestration in the Paluxy formation at the continuum scale. Additional simulations were carried out using BET surface areas collected from the literature and geometric surface areas. Simulations were run for 7300 days and mineral volume fractions and effluent ion concentrations tracked and compared. Variations in mineral surface areas measured from images are within 1 order of magnitude and yield similar simulation results, indicating the impact of image resolution on simulated reactions and reaction rates is minimum for the resolutions and sample considered. In comparison, surface areas obtained from BET and geometric approaches are 1-5 orders of magnitude higher than image-obtained surface areas and result in greater simulated reaction rates and extents. Minerals with high reaction rates (calcite and siderite) are most impacted by surface area values at short times where simulated mineral volume fractions at longer times agree relatively well, even for simulations with several orders of magnitude variation in surface area. Phases with lower reaction rates, such as K-feldspar and muscovite, are predominantly impacted over longer times where variations in surface areas impact reaction extents and porosity evolution.

333435

Keywords: Reactive transport modeling; Image resolution, Mineral surface area; Geochemical reactions

3637

38

1. Introduction

Reactive transport modeling has been used extensively to enhance understanding of geochemical reactions and transport phenomena happening in a wide variety of surface and subsurface systems (Steefel et al., 2005, 2013; Pallud et al., 2007; Boana et al., 2014; Li et al., 2017; Steefel, 2018; Maher and Navarre-Sitchler, 2019). For example, reactive transport simulations have been used to enhance the understanding of the fate of contaminants in porous media (Sen et al., 2006; Apul et al., 2007; Xu et al., 2010; Essaid et al., 2015; Schmidt et al., 2019), to evaluate CO₂-induced dissolution and precipitation reactions and corresponding porosity and permeability evolution in subsurface environments (White et al., 2005; Audigane et al., 2007; Bacon et al., 2009; Meakin et al., 2009; Aradóttir et al., 2012; Nogues et al., 2013; Connell et al., 2015; Deng et al., 2015; Ng et al., 2015; Steefel et al., 2015; Navarre-Sitchler et al., 2011 and 2017; Bo Guo et al., 2018; Liu et al., 2019; Miao et al., 2019; Schmidt et al., 2019; Elkady and Kovscek, 2020), and to simulate biogeochemical process such as uranium bioremediation (Scheibe et al., 2009; Yabusaki et al., 2011; Martinez et al., 2014; Grandclerc et al., 2018; Shultz et al., 2018; la Cecilia et al., 2019). Models have the advantage of being able simulate the evolution of a system beyond laboratory time scales where models are developed based on experimental systems and validated with experimental observations (Martens et al., 2012; Salehikhoo et al., 2013; Beckingham et al., 2017).

While reactive transport models are widely used, simulating mineral reactions is challenging not only due to the complexity of the reactions, but also uncertainties in estimating model parameters. In addition, changes in mineral porosity, permeability and reactive surface may occur as reactions progress (Gouze and Luquot, 2011; Qajar, 2012; Qajar and Arns, 2016; Beckingham et al., 2017; Yang et al., 2018; Altree-Williams et al., 2019), which could impact the modeling results. Mineral reaction rates are commonly estimated using a rate law based on transition state theory (TST) (Lasaga, 1981, 1984; Aagaard and Helgeson, 1982) where the reaction rate is given by,

$$R_m = A_m k_m [f \Delta G_r] \tag{1}$$

where A_m is mineral reactive surface area, k_m is mineral rate constant, and $f\Delta G_r$ is the thermodynamic driving force for the reaction (Stefeel et al., 2015). While the thermodynamic aspects of mineral reactions are generally well understood, difficulties exist in estimating parameters for mineral nucleation and growth, rate constants in non-

ideal conditions including high temperatures and pressures, and mineral reactive surface area (SA) (Hellevang et al., 2013; Black et al., 2015; Bourg et al., 2015). These variations may result in differences in simulated results. Estimated rate constants typically vary by one order of magnitude (Black et al., 2015), whereas variations in reported mineral surface area values span several orders of magnitude (Black et al., 2015; Bourg et al., 2015).

Mineral surface areas are typically measured in the laboratory or estimated based on geometry. In the laboratory, mineral specific surface area is often measured using the Brunauer–Emmett–Teller (BET) adsorption method (Brunauer et al., 1938). Surface areas estimated based on a geometry approximation typically assume mineral grains are smooth, spherical, and of a uniform size (Anbeek, 1992; Gunter et al., 2000; Noiriel et al., 2009). When clay minerals are present, an additional smaller grain size might be assumed (White et al., 2005; Alemu et al., 2011; Beckingham et al., 2016). These surface areas may or may not be additionally adjusted by roughness and scaling factors varying one to three orders of magnitude to account for surface roughness and variations in reactive site density (Bourg et al. 2015).

Imaging has emerged as powerful tool to quantify mineral properties including mineral abundance, mineral accessibility and mineral accessible surface area (defined in section 2.2.2.1) (Peters, 2009; Landrot et al. 2012; Beckingham et al., 2016 and 2017; Qin and Beckingham, 2019). In this approach, images of mineral thin sections captured using scanning electron microscopy (SEM) under backscatter electron (BSE) mode are segmented into discrete mineral phases utilizing energy dispersive X-ray spectroscopy (EDS) elemental maps. Mineral accessibility is calculated from 2D BSE images by first identifying connected porosity and then corresponding adjacent mineral surfaces (Beckingham et al., 2017, Qin and Beckingham, 2019). This is then combined with 3D X-ray computed tomography (CT) images to calculate pore connectivity in three dimensions and used to infer three-dimensional mineral accessible surface areas (Landrot et al. 2012, Beckingham et al., 2017, Qin and Beckingham, 2019). The required images can be captured over a wide range of resolutions where the impact of image resolution on the quantification of mineral abundance and mineral accessible

surface area was assessed in Qin and Beckingham (2019). This analysis revealed mineral volume fractions calculated for a sandstone sample using images with resolutions at 0.34 µm to 5.71 µm agreed relatively well and mineral accessible surface areas varied up to 1 order of magnitude (Qin and Beckingham, 2019). Image-obtained accessible surface areas of calcite, siderite and K-feldspar decreased with decreasing resolution while the accessible surface area of quartz increased with decreasing image resolution. It was also noted that images with even higher resolutions, however, are needed to adequately depict clay minerals and phases with small-scale features (e.g. muscovite) (Qin and Beckingham 2019).

Imaging and image analysis are powerful means of quantifying mineral properties to inform reactive transport simulations, including accessible surface areas where it has been found that accessible surface area better reflects mineral reactive surface area in porous media and better reproduces observed dissolution rates (Beckingham et al. 2017). However, capturing images under high resolutions and processing high resolution images is time-consuming and may have high computational costs. The necessity of this time and resource investment to improve simulation of mineral reactions and reactions rates, however, is not well understood. This work evaluates variations in simulated mineral reactions and reaction rates using mineral surface areas obtained from images with varying resolution and values obtained using traditional approaches. Mineral surface areas measured from image analyses in Qin and Beckingham, (2019) were used here to evaluate the impact of image resolution on simulated mineral reactions extents and reaction rates. These simulations are compared to those utilizing BET mineral surface areas from the literature and geometric surface areas (GSA) calculated assuming two uniform spherical sizes, one for clay minerals and the other for non-clay minerals. Simulations compare variations in mineral reactions, reaction rates, and porosity over short and long times.

126127

128

129

130

101

102

103

104

105

106

107

108

109

110

111

112

113

114

115

116

117

118

119

120

121

122

123

124

125

2. Materials and methods

2.1 Sample characterization

Sandstone samples extracted from the Paluxy formation at the Kemper County

power plant, Kemper County, Mississippi, a prospective pilot CO₂ injection plant, were considered in this study. These samples were also the focus of previous analysis in Qin and Beckingham (2019) where bulk samples were collected from well MPC 10-4 #1 and well MPC 34-1 at depths from 1539 m to 1624 m. XRD analysis was performed on powdered samples and SEM BSE images of thin sections were captured for image analyses (Qin and Beckingham, 2019). The mineralogy, mineral abundances, and mineral volume fractions determined from 2D BSE images of a thin section of the rock sample extracted at the depth of 1539 m (Qin and Beckingham, 2019) were used here and are reported in Table 1. Mineral abundances are defined as mineral volume percentage without pore space (m³ mineral volume/ m³ total mineral volume) and mineral volume fractions are defined as mineral volume percentage within the porous medium (m³ mineral volume/ m³ total porous medium volume). Mineral rate constant values (Table 1) were interpolated following Beckingham et al. (2016) at anticipated formation conditions post CO₂ injection corresponding to a temperature of 50°C and pH of 3.5.

Table 1. Mineral abundances calculated from a $0.34~\mu m$ 2D SEM image in Qin and Beckingham (2019) and corresponding mineral volume fractions and rate constants for reactive transport simulations. Rate constant values: quartz (Brady and Walther, 1990), K-feldspar (Van Hees et al., 2002), calcite (Alkattan et al., 1998), smectite (Amram and Ganor, 2005), muscovite (Knauss and Wolery, 1988; Oelkers et al., 2008), siderite (Golubev et al., 2009).

Mineral	Chemical formula ^a	Abundances (%)	Volume fraction (%)	Log k (mol/m²/s) ^b
Quartz	SiO ₂	76.45	57.46	-11.6
K-feldspar	KAlSi ₃ O ₈	3.5	2.63	-11.65
Calcite	CaCO ₃	9.63	7.24	-4.21
Smectite	$(Ca_{0.2}Na_{0.15})K_{0.2}(Fe_{0.29}Mg_{0.9}) $ $(Al_{1.25}Si_{3.75})(OH)_{6.5}$	8.23	6.19	-13.35
Muscovite	KAl ₂ (AlSi ₃ O ₁₀)(OH) ₂	0.31	0.23	-12.67
Siderite	$Fe_{0.9}Mg_{0.1}CO_3$	1.98	1.41	-5.69

^a Smectite and siderite chemical formula are determined from EDS linescan.

2.2 Reactive transport simulations

b Mineral rate constants correspond to a temperature of 50°C and pH of 3.5.

2.2.1 Model description

Continuum scale reactive transport simulations were built and carried out using CrunchFlow (Steefel et al., 2015). The model system (Fig. 1) consisted of a 3 cm long mineral cell in equilibrium with formation brine proceeded by a cell containing a constant partial pressure of CO₂ in equilibrium with formation brine that acts as a constant source of CO₂-saturated brine throughout the simulations. The mineral composition in the mineral cell was based on the mineral volume fractions determined from analysis of thin sections in Qin and Beckingham (2019) and given in Table 1. The initial formation brine chemistry (Table 2) was determined by simulating minerals equilibrating with 1 mol/(kg fluid) NaCl brine for 100,000 years where the resulting initial pH, based on charge balance, is 8.81.





Fig. 1. Diagram of the simulation system.

171 Table 2. Simulated brine chemistry of the Paluxy formation.

Ion	Concentration (mol/kg fluid)
Na ⁺	1.00E-00
Cl-	1.00E-00
Ca^{2+}	7.00E-04
Mg^{2+}	5.88E-07
Fe ²⁺	5.64E-05
K^+	1.08E-04
Al^{3+}	1.08E-06
SiO ₂ (aq)	8.82E-04
CO ₂ (aq)	7.65E-04
рН	8.81

The estimated temperature and pressure at the sample depth, 1539 m, is 50 °C and 163 bar, calculated based on a temperature gradient of 25 °C/km and surface temperature of 10 °C and pressure gradient of 105 bar/km (Bachu, 2000; Crandell et al., 2009). These conditions control the solubility of CO₂ in the formation brine, calculated

in CrunchFlow using the Duan and Sun model (Duan and Sun, 2003). These conditions result in a CO₂ saturated brine with a pH of 3.5. In the simulations, the CO₂ saturated brine flowed through the mineral cell at a constant flowrate of 1 m/day and the evolution of major ions and mineral volume fractions tracked. Precipitation of potential secondary mineral phases was also considered where the potential precipitating phases were selected using the database sweep option in CrunchFlow.

2.2.2 Mineral surface area

Table 3. Mineral surface area values used in reactive transport simulations. High and low resolution correspond to 0.34 μm and 5.71 μm resolution SEM images analyzed in Qin and Beckingham (2019), respectively. The surface area of quartz, K-feldspar, calcite and siderite were determined from images while the surface area of smectite and muscovite are from Beckingham et al. (2017) and Knauss and Wolery (1989), respectively. High and low BET literature refer to BET measured surface area values collected from the literature: quartz (Brady and Walther, 1989; Tester et al., 1994), K-feldspar (Bunsenberg and Clemency, 1976; Gautier et al., 1994), calcite (Papadopoulos and Rowell, 1988; Cubillas et al., 2005), smectite (Kennedy et al., 2002; Metz et al., 2005), muscovite (Caseri et al., 1992; Knauss, 1989), siderite (Shan and Guo, 2013; Erdem and Ozverdi, 2005). GSA_{RF} refers to geometric surface area multiplied by a roughness factor, *RF*, of 10 to account for surface roughness and GSA_{SF} is GSA_{RF} divided by a scaling factor, *SF*, of 10 to account for surface site reactivity.

	Surface area values (m ² /g)					
Mineral	high resolution imaging	low resolution imaging	GSA _{RF} = GSA*RF	$\begin{aligned} GSA_{SF} &= \\ GSA_{RF}/SF \end{aligned}$	high BET literature	low BET literature
Quartz	2.56E-2	4.59E-2	1.18E-1	1.18E-2	1.11E-1	2.25E-2
K-feldspar	2.62E-2	1.49E-2	1.22E-1	1.22E-2	1.52E+0	1.12E-1
Calcite	1.10E-2	7.79E-3	1.15E-1	1.15E-2	1.64E+0	1.39E-2
Smectite	9.33E+0	9.33E+0	8.56E+1	8.56E+0	8.00E+2	3.40E+1
Muscovite	2.38E+0	2.38E+0	1.11E-1	1.11E-2	3.40E+0	1.10E+0
Siderite	1.77E-2	1.72E-2	7.90E-2	7.90E-3	5.17E+1	2.67E+0

Six different sets of surface area (Table 3) were determined and used in a systematic series of reactive transport simulations. This included two sets of accessible mineral surface areas determined using images at different resolutions, two sets of geometric surface areas with and without a scaling factor, and two sets of specific surface areas determined from BET analyses (Table 3). In CrunchFlow, mineral surface areas are updated as reactions proceed, based on the following relationships for dissolution and

204 precipitation:

Dissolution:
$$A = A_{initial} \left(\frac{\phi_m}{\phi_m^{initial}}\right)^{\frac{2}{3}} \left(\frac{\phi}{\phi^{initial}}\right)^{\frac{2}{3}}$$
 (2)

Precipitation:
$$A = A_{initial} (\frac{\emptyset}{\emptyset^{initial}})^{\frac{2}{3}}$$
 (3)

where A is the reactive surface area, Φ is the porosity and Φ_m is the individual mineral volume fraction.

2.2.2.1 Image obtained accessible surface area

Mineral accessible surface areas used here were calculated using a multi-scale 2D and 3D imaging approach in Qin and Beckingham (2019). Accessible surface was defined as mineral surfaces adjacent to connected pore spaces. In Qin and Beckingham (2019), these image-obtained accessible surface areas were calculated using 2D SEM images of varying resolution, 0.34 μm to 5.71 μm. Here, values from the highest (0.34 μm) and lowest (5.71 μm) image resolution were considered. It should be noted that even the image resolution of 0.34 μm was not sufficient to calculate surface area of smectite and muscovite, thus the surface area of smectite determined using FIB-SEM imaging from Beckingham et al. (2017) and BET measured value for muscovite from Knauss and Wolery (1989) were used here. The sets of image obtained surface areas are given in Table 3 and referred to as high resolution imaging and low resolution imaging.

2.2.2.2 Geometric specific and effective surface areas

Geometric surface areas were calculated from the experimentally measured average grain diameter for non-clay and clay minerals assuming spherical grains. The average grain diameters were determined from grain size distributions measured by Weatherford Labs for 7 samples from the Paluxy formation at depths of 1540 m, 1541 m, 1547 m, 1549 m, 1551 m, 1556 m, and 1562 m. The corresponding average grain diameters were 191.8 µm for non-clay minerals and 0.3 µm for clay minerals (details in supplementary materials). To account for mineral surface roughness, the spherical surface areas based on these grain diameters were multiplied by a roughness factor (RF) of 10 where the resulting surface area corresponds to an estimate of a specific surface

area. A second set of surface area values reflecting limitations to surface reactivity, as would occur from reduced accessibility or only a fraction of the surfaces being reactive, were also calculated by dividing rough surface areas by a scaling factor, *SF*. Scaling factors typically range one to three orders of magnitude (White and Peterson 1990) where a scaling factor of 10 is used here. The resulting surface area is an estimate of an effective surface area where values for both surface areas are given in Table 3 and are referred to as GSA_{RF}, the geometric surface area adjusted for surface roughness with a roughness factor, and GSA_{SF}, the rough geometric surface area adjusted by the scaling factor that accounts for both surface roughness and surface site reactivity.

2.2.2.3 Literature specific surface area

Mineral specific surface areas measured using the BET method (Brunauer et al., 1938) in previous studies were collected from the literature and used here. For a given mineral phase, BET surface areas vary up to 4 orders of magnitude (Black et al., 2015; Bourg et al., 2015) depending on sample source, sample condition, adsorption method used, etc. Here, mineral specific surface areas reported in the literature were collected and the highest and lowest measured values on pure mineral samples were selected. These values are referred as the high BET literature and low BET literature in Table 3.

3. Results

Simulations first consider the impact of image resolution on simulated mineral reactions and reaction rates by comparison of simulations using accessible surface areas obtained from the highest and lowest resolutions images in Qin and Beckingham (2019). Then, this is further compared with simulations using surface area values more easily obtained including geometric surface areas based on average grain diameters and BET obtained specific surface areas. All simulations consider the evolution of mineral volume fractions, ion concentrations, pH, porosity and surface area. For all the simulation results, time starts from negative values, indicating the state of the system before CO₂ injection. At a time of 0 hours, CO₂-saturated brine enters the system. The purpose of this is to better reflect some of the changes happening at early times.

3.1 Imaging-based simulations

3.1.1 Mineral volume fractions

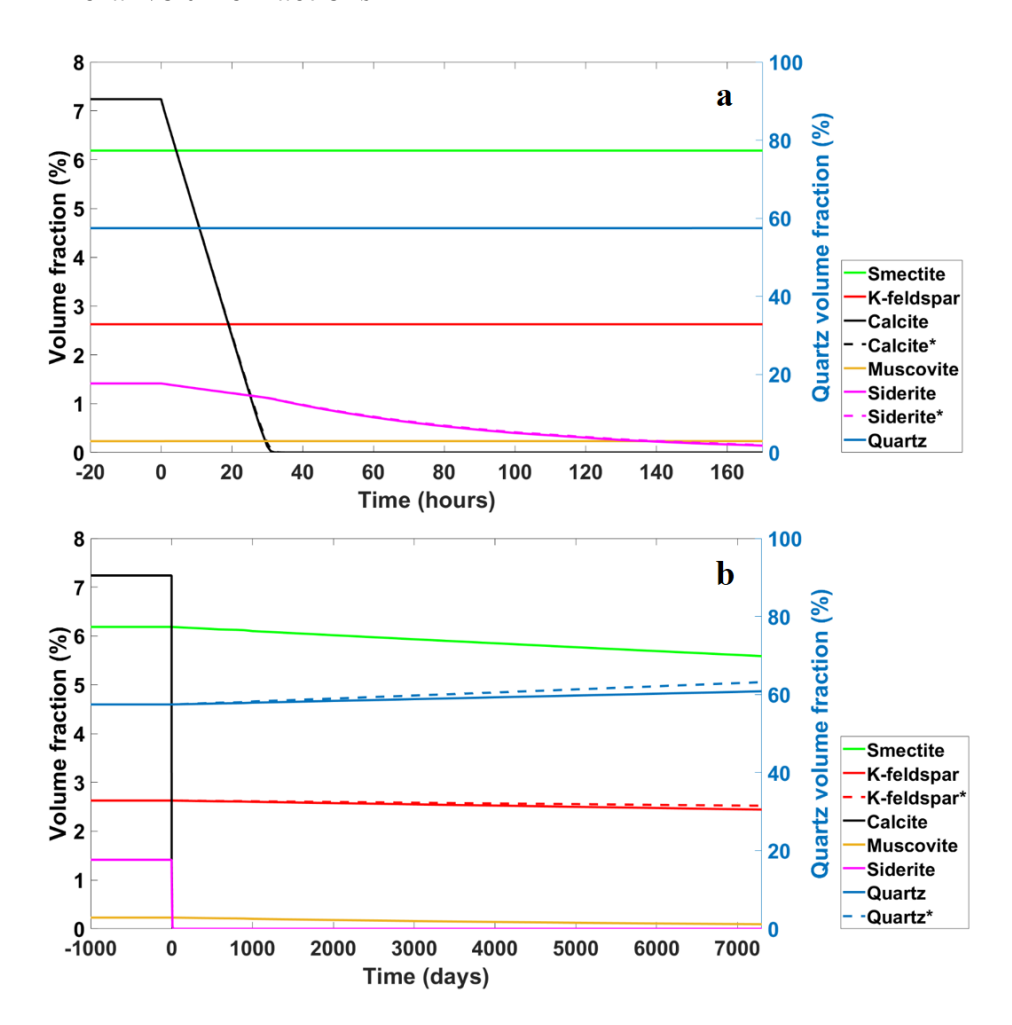


Fig. 2. Simulated evolution of mineral volume fraction using imaging-based accessible surface areas depicting (a) the first 170-hours and (b) the entire 7300-day simulation. Solid lines are results of simulations using surface areas from high resolution images (0.34 μ m), dashed lines, also labeled with a *, indicate simulation results using surface areas from low resolution images (5.71 μ m). A single solid line is shown for minerals with no discernable difference between the two simulations.

The evolution of mineral volume fractions from simulations carried out using imaging-based accessible surface area are shown in Fig. 2. Here, surface areas vary by less than one order of magnitude for all minerals and result in very small variations in mineral volume fractions where discernable differences only occur at longer times (Fig. 2b). In these simulations, CO₂ saturated brine enters the system at 0 hours and leads to

dissolution of the two carbonate phases - calcite and siderite, while the other mineral phases remain relatively stable during the first 170 hours (Fig. 2a). Calcite rapidly dissolves and it is close to depletion around 30 hours in both simulations, where the calcite volume fraction decreases from 7.23% to 0.13% in the simulation using the accessible surface area from high resolution images (solid lines). In simulations using the accessible surface area from low resolution images, the calcite volume fraction decreases to 0.19% (dashed lines) at 30 hours. Compared to calcite, siderite dissolution is relatively slower and the dissolution rate slightly increases as calcite nears depletion. During the first 170 hours, the volume fraction of siderite decreases from 1.41% to 0.14% and to 0.15% in simulations using accessible surface area from high and low resolution images, respectively. Volume fractions of the other mineral phases change by less than 0.01%.

At longer times, quartz precipitates while smectite, K-feldspar and muscovite dissolve. There is little variation between in the two simulations using the different accessible surface area values. Quartz precipitates in both simulations due to the low pH and high SiO₂(aq) concentrations. It should be noted that previous works have suggested chalcedony, a polymorph of quartz, is the more likely precipitating phase (Audigane et al., 2007; Pham et al., 2011) but this was not observed in this simulation. Quartz surface areas vary within one order of magnitude where a higher accessible surface area, from the lower resolution images, results in a small increase in simulated precipitation, from 57.46% to 63.17% (dashed line) in comparison to the increase to 60.82% (solid lines) in the simulation using the accessible surface area from high resolution images. The volume fraction of K-feldspar decreases from 2.63% to 2.44% and 2.52% in simulations using accessible surface areas from high (solid lines) and low (dashed lines) resolution images, respectively. The volume fraction of smectite decreases from 6.18% to 5.59% and muscovite decreases from 0.23% to 0.09%. As these surface areas cannot be determined from imaging, the same BET surface area values are used for smectite and muscovite in these simulations and therefore no discernable differences in volume fractions of these mineral phases occur.

3.1.2 Ion concentration and pH

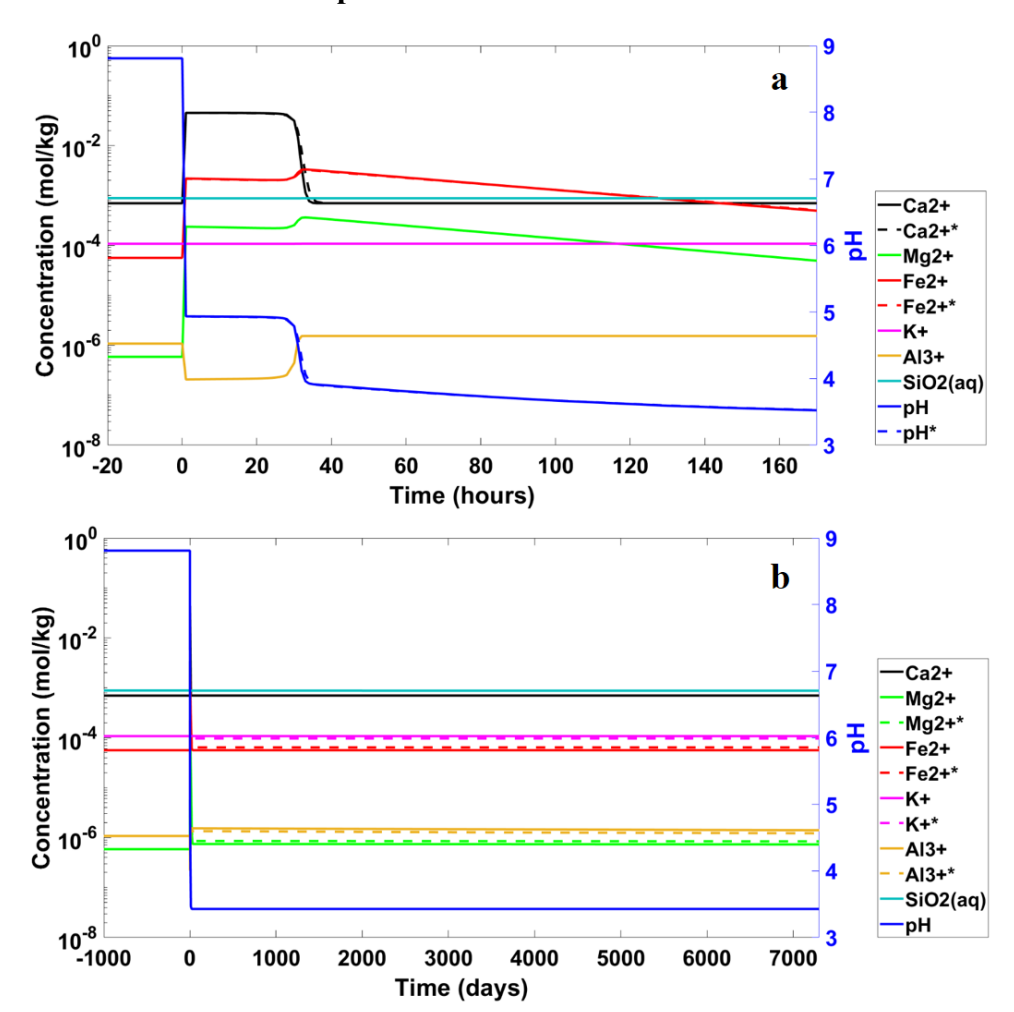


Fig. 3. Simulated evolution of major ion concentrations and pH over a) 170 hours and b) 7300 days for simulations using imaging-based accessible surface areas. Solid lines are results of simulations using surface area from high resolution images (0.34 μ m), dashed lines labeled with superscript * correspond to results of simulations using surface area from lower resolution images (5.71 μ m).

The evolution of major ion concentrations and pH are shown in Fig. 3. The introduction of CO₂-saturated brine with a pH of 3.5 at 0 hours results in a decrease in the pH in the mineral cell from the initial pH of 8.8 and increases in the concentrations of calcium, magnesium and iron as calcite and siderite dissolve (Fig. 3a). Calcite dissolution rapidly buffers the pH to 4.9. The decrease of aluminum ion concentration between 0 to 35 hours is most likely to be explained by the high super-saturation of muscovite (Fig. S1 in supplementary material). During this period, muscovite is super-

saturated and a small amount of precipitation that is not discernable on the plot (Fig. 2a) occurs. After 35 hours, when calcite is completely consumed, the pH reduces towards 3.5. These conditions no longer favor muscovite precipitation, so the aluminum concentration returns to the background level. No observable changes occur for potassium and SiO₂(aq) at early times. At longer times, slow dissolutions of smectite and muscovite keep the aluminum and magnesium concentration levels slightly elevated above background levels. The concentrations of other ions remain stable at background levels.

Overall, the differences in pH and major ion concentrations are small in these two simulations using accessible surface areas from different resolution images. Only small variations in the evolution of pH and calcium concentration are observed around 35 hours (Fig. 3a). At longer times, slight variations in magnesium, iron, potassium and aluminum can be observed. The good agreement between simulation results indicate that the variations in mineral accessible surface areas within one order of magnitude caused by differences in image resolution only have a small impact on simulated mineral reactions and reaction rates.

3.1.3 Porosity

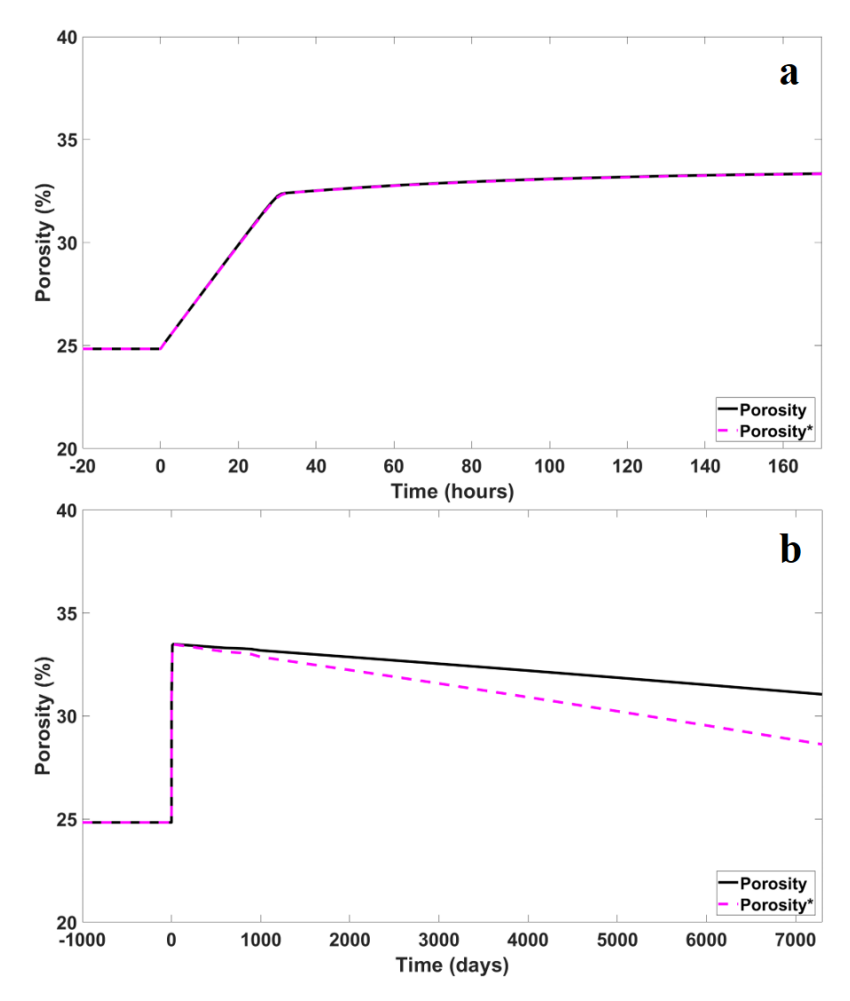


Fig. 4. Simulated porosity evolution over a) 170 hours and b) 7300 days for simulations using imaging-based accessible surface areas. Black solid lines are results of simulations using surface area from high resolution images (0.34 μ m), magenta dashed lines, labeled with *, indicate results of simulations using surface areas from lower resolution images (5.71 μ m).

The simulated porosity evolution for simulations using image obtained surface areas are shown in Fig. 4. At early times, porosity increases following CO₂-saturated brine entering the system at 0 hours. In the first 170 hours, the porosity increases from 25% to 32% in both simulations (Fig. 4a), mainly due to the dissolution of calcite. The porosity then further increases from 32% to 33% due to siderite dissolution. At later times, quartz slowly precipitates, resulting in a decrease in porosity from 33% to 31% in the simulation using accessible surface areas from the high resolution image (solid lines) and decreases to 29% in the simulation using accessible surface areas from the low resolution image (dashed lines). There is no discernable difference in porosity

evolution over the first 170 hours (Fig. 4a) and the variation in long-term porosity evolution between the two simulations is small (Fig. 4b).

3.2 Non-imaging based simulations

In this section, results of simulations using BET specific surface areas and geometric specific and effective surface areas are presented and compared with results from simulations using image obtained accessible surface areas.

3.2.1 Mineral volume fractions

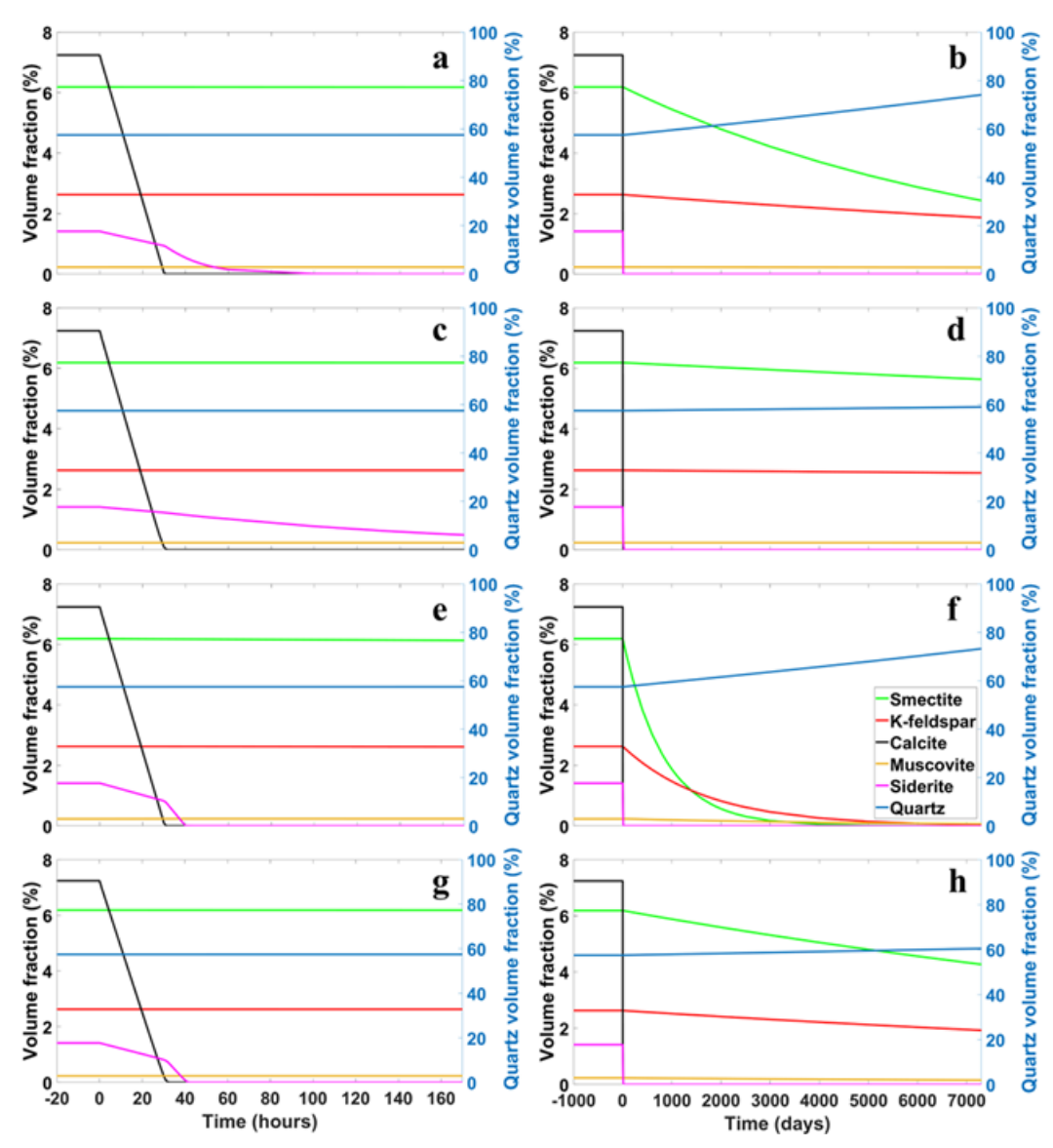


Fig. 5. Simulated evolution of mineral volume fractions using (a-b) geometric specific surface areas that account for surface roughness (GSA_{RF}), (c-d) geometric effective surface areas

accounting for surface roughness and reactive site density (GSA_{SF}), (e-f) high BET literature specific surface areas, and (g-h) low BET literature specific surface areas.

370

371

372

373

374

375

376

377

378

379

380

381

382

383

384

385

386

387

388

389

390

391

392

393

394

395

396

397

368

369

The evolution of mineral volume fractions for simulations using geometric and BET specific surface areas are shown in Fig. 5. Following introduction of CO₂ saturated brine (0 hours), calcite and siderite dissolve at early times. The dissolution of siderite in simulations using geometric specific surface areas (Fig. 5a), e.g. those that account for surface roughness, is slightly faster than in the two imaging-based simulations (Fig. 2a). In simulations that use geometric effective surface areas (Fig. 5c), the evolution of siderite volume fraction agrees relatively well with the two imaging-based simulations. Simulations carried out using literature BET specific surface areas have the fastest siderite dissolution rates and earliest siderite consumption times. In comparison to the accessible surface areas obtained from imaging, the geometric specific surface areas and BET specific surface area of siderite are 1 to 4 orders magnitude higher (Table 3). As expected, a higher surface area leads to a faster dissolution rate, particularly after consumption of calcite (30 hours) where the pH is lower. There is little variation in siderite dissolution rates in simulations using the highest surface areas, those from BET analyses (Fig. 5e and g). While the high BET surface area is more than one order of magnitude larger than the low BET surface, this difference does not further increase the consumption rate of siderite. In comparison, there are more than 2 orders of magnitude variation in calcite surface areas among all simulations but no distinct differences in the calcite consumption rate can be observed. Little variation in volume fractions of the other four minerals occurs within the first 170 hours, in agreement with simulation results using image-obtained surface areas.

Over 7300 days, simulations that use higher surface areas (geometric and BET specific surface areas) have faster dissolution rates compared to simulations using image-obtained accessible surface areas (Fig. 2), but to varying extents. In the two imaging–based simulations (Fig. 2b), the smectite volume fraction decreases from 6.18% to 5.58% at 7300 days. In simulations using geometric specific and effective surface areas (Fig. 5b and d), volume fractions of smectite decrease from 6.18% to 2.43% and

5.64% and decrease to 0.001% and 4.27% in simulations using high and low literature BET specific surface areas (Fig. 5f and h) where increased depletion is coupled to higher surface area values. In simulations using image-obtained surface areas (Fig. 2b), the volume fraction of K-feldspar decreases from 2.63% to 2.44% and 2.52% at 7300 days. With the higher surface areas used here (Fig. 5), the volume fraction of K-feldspar decreases from 2.63% to 1.87% and 2.54% in simulations using geometric specific and effective surface areas (Fig. 5b and d) and decreases to 0.04% and 1.93% in simulations using literature BET surface areas (Fig. 5f and h) where increased depletion is also coupled to higher surface area values. Precipitation of quartz occurs to varying extents in all four simulations, driven by the low pH and abundant SiO₂(aq) in the flowing fluid. The volume fraction of quartz increases from 57.46% to 74.09% and 58.99% in simulations using geometric specific and effective surface areas (Fig. 5b and d) and 73.21% and 60.42% in simulations using high and low literature BET surface areas (Fig. 5f and h).

3.2.2 Ion concentration and pH

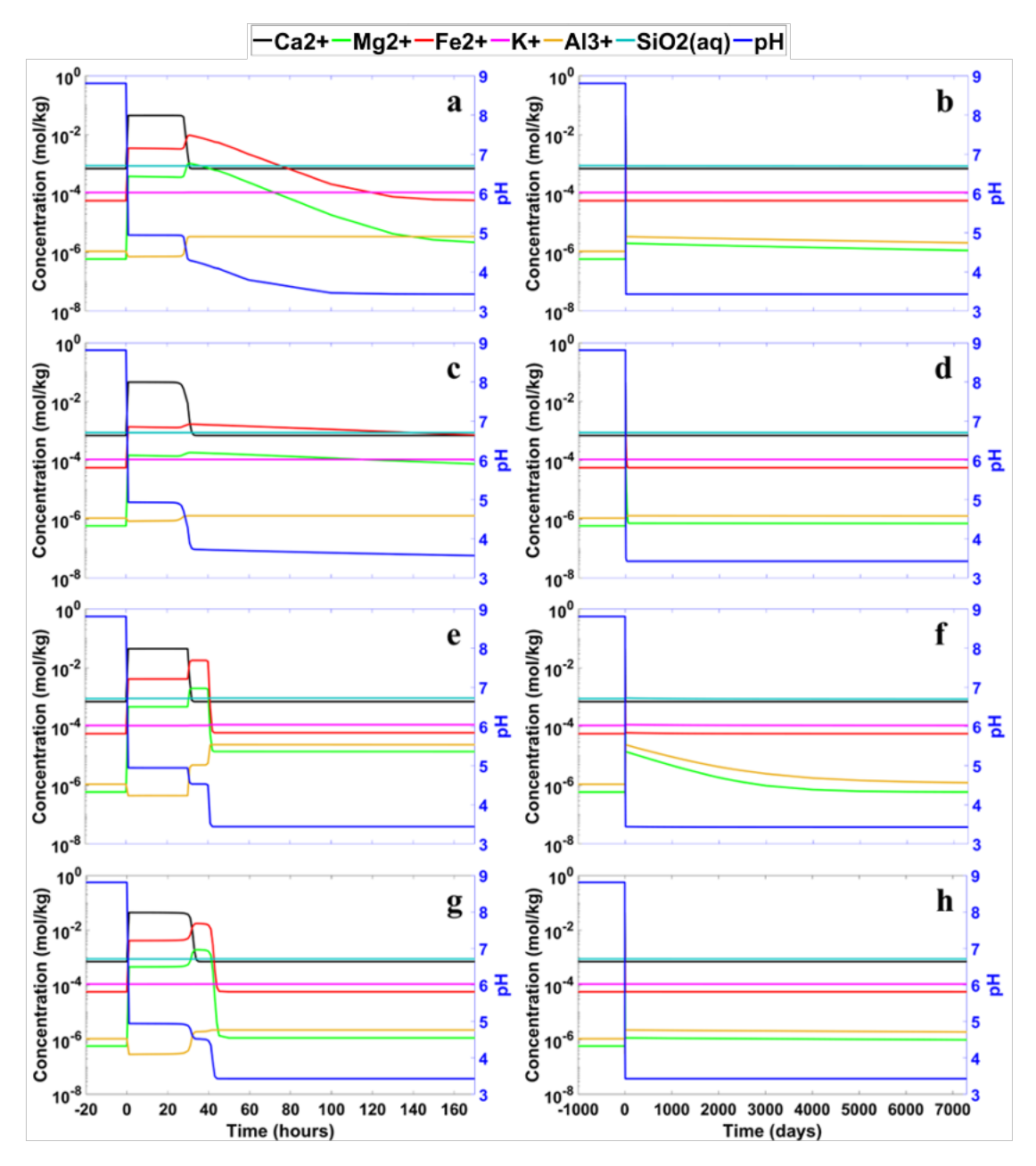


Fig. 6. Simulated evolution of major ion concentrations and pH for simulations using (a-b) geometric specific surface areas (those that reflect surface roughness, GSA_{RF}), (c-d) geometric effective surface areas (those accounting for surface roughness and adjusted by a scaling factor to reflect reactive site density, GSA_{SF}), (e-f) high BET literature specific surface areas, and (g-h) low BET literature specific surface areas.

Ion concentrations for simulations using geometric surface areas and BET surface areas from the literature are shown in Fig. 6. Variations in ion concentrations among simulations, and with simulation results using image-obtained accessible surface areas

(Fig. 3), are readily apparent. As CO₂-saturated brine enters the system at 0 hours, calcium, magnesium and iron concentrations increase as calcite and siderite dissolve. From 0 to 30 hours, dissolution is dominated by calcite and evident here through high calcium concentrations. While there are two orders of magnitude variation in geometric and BET surface areas, this only results in small variations in simulated calcium ion concentrations. As calcite approaches depletion, siderite dissolution increases and becomes dominant which leads to further increases in magnesium and iron concentrations after 30 hours. Variations in magnesium and iron occur between simulations, resulting from differences in siderite dissolution rates. Although there is no discernable difference in siderite volume fractions (Fig. 5e and g), the concentration level of magnesium is higher for simulations using higher BET specific surface areas (Fig. 6e and g). pH closely follows the dissolution of calcite, buffered by calcite dissolution to 4.9 during 0 to 30 hours and then decreasing to 3.5 after 30 hours when calcite is depleted. The evolution of aluminum concentration follows the change of muscovite saturation index (Fig. S1 in supplementary material), where muscovite initially precipitates and decreases aluminum concentrations and then dissolves and increases aluminum concentrations.

Variations in concentration tied to surface areas can be observed where higher surface areas result in higher reaction rates and associated ion concentrations. In comparison to simulations using image-obtained accessible surface areas at early times, calcium concentrations return to background levels quicker in comparison to in simulations using geometric specific surface area and high literature BET specific surface area where calcite has a higher surface area by 1-2 orders of magnitude and is depleted more rapidly. This also impacts the evolution of pH, largely controlled by calcite dissolution, and magnesium and iron, where the dissolution rate of siderite increases after calcite depletion. Higher concentrations of iron, magnesium and aluminum and more rapid changes in their concentrations can be observed in the simulations using the higher surface area values.

At longer times, elevated levels of magnesium and aluminum can be observed, reflecting dissolution of smectite and muscovite. In terms of the surface area values

used in the simulations, higher surface areas lead to faster dissolution and therefore higher concentrations of magnesium and aluminum in the first 5000 days. After 5000 days, however, there is little variation in magnesium and aluminum concentrations among simulations until smectite and muscovite approaching depletion (Fig. 5f and Fig. 6f) where concentrations approach background levels. In comparison, potassium and iron have higher background concentrations, such that the release of potassium and iron due to slight mineral dissolution (e.g. K-feldspar and smectite) do not largely impact potassium and iron concentrations. Overall, variations in ion concentrations among all simulations, including those using image-obtained accessible surface areas, are readily apparent at early times (170 hours) and small at longer times. Simulated ion concentrations after ~500 days agree well for simulations using low BET specific surface areas and geometric specific and effective surface areas, After ~5000 days, simulated ion concentrations for simulations using high BET surface areas agree well with other simulation results.

3.2.3 Porosity

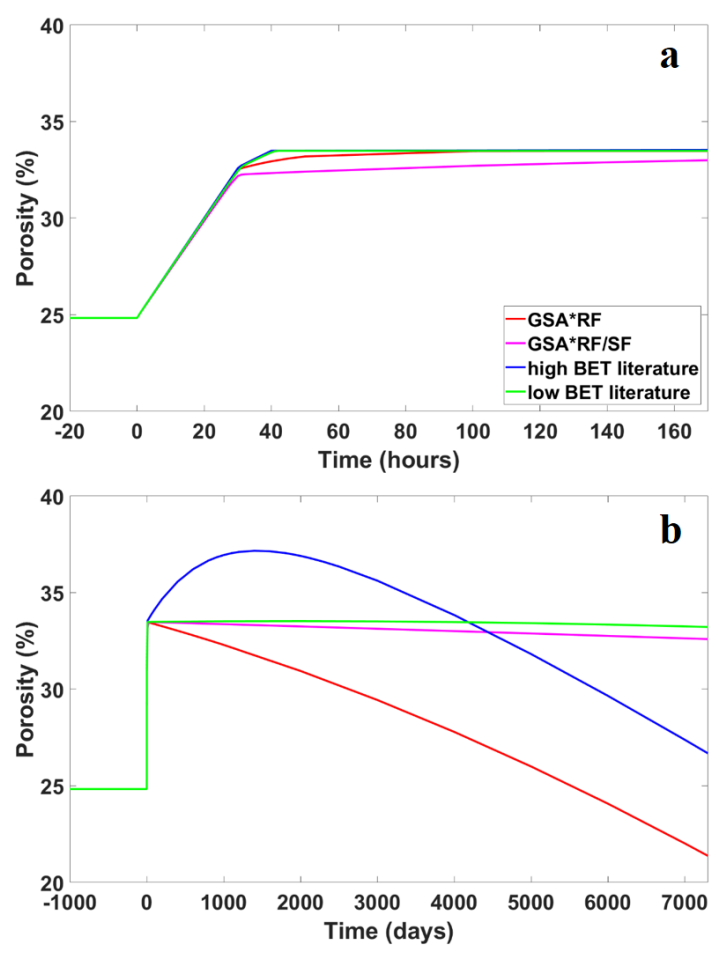


Fig. 7. Simulated porosity evolution using geometric specific and effective surface areas and literature BET specific surface areas.

The simulated evolution of porosity for simulations using geometric surface areas and BET specific surface areas are shown in Fig. 7. Rapid dissolution of carbonate minerals following introduction of CO₂-saturated brine at 0 hours results in an increase in porosity from 25% to around 33% in all four simulations (Fig. 7a). While the calcite and siderite surface area values in the simulations vary by 2 and 4 orders of magnitude, respectively, the overall difference in porosity increase is small in 170 hours.

Over longer times, variations in surface area values result in larger differences in the simulated evolution of porosity. In simulations that use the highest BET surface area values from the literature (green line), the porosity further increases to 37% due to dissolution of smectite and K-feldspar. In all simulations, after the initial porosity increase, porosity decreases as little additional dissolution occurs and SiO₂ precipitates.

The extent of precipitation, and corresponding change in porosity, varies between simulations where the porosity decreases from 33% to 21% in the simulations that use geometric specific surface areas (red lines) and decreases to 27% in the simulations that use high BET literature specific surface area values (green lines). This is higher than the decrease to 31% and 29% in simulations using surface areas from high- and low-resolution images, respectively. In simulations where smaller surface areas of SiO₂ are used, geometric effective surface areas and low BET specific surface areas (magenta and green lines), the porosity only decreases slightly over 7300 days which better agrees with results from simulations using image obtained accessible surface areas.

3.3 Mineral surface area evolution

Here, the simulated evolution of mineral surface areas is tracked where surface areas are updated in CrunchFlow using Equations 2 and 3 for dissolution and precipitation, respectively. Mineral surface area evolutions in the first 170 hours are presented here for calcite and siderite, while the surface areas for the other four mineral phases are minor and given in Fig. S2 in the supplementary materials. At longer times, calcite and siderite are completely dissolved and thus only the surface area evolution of the remaining phases, quartz, K-feldspar, smectite and muscovite, are presented here.

3.3.1 Short term surface area evolution

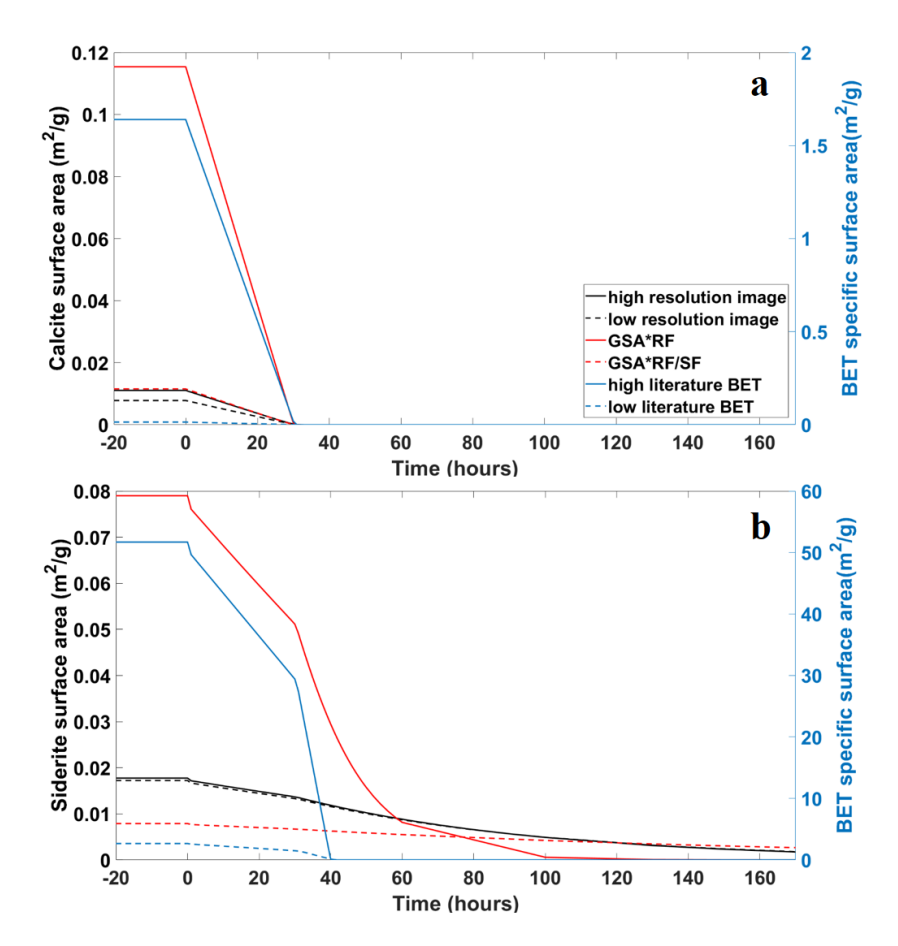


Fig. 8. Simulated mineral surface area evolution of carbonate minerals over the first 170 hours: (a) calcite and (b) siderite. The evolution of BET specific surface areas (blue lines) are plotted on the right y-axis.

The simulated evolution of mineral surface area for calcite and siderite for all six simulations are shown for the first 170 hours in Fig. 8. There are 2 orders of magnitude variation in calcite surface areas where the simulated evolution of surface areas that are initially higher decreases faster than surface areas that are initially lower. In all simulations, the surface area of calcite decreases to 0 around 30 hours, reflecting calcite depletion (Fig. 8a). A similar phenomenon can be observed for siderite, where initial surface area values span 4 orders of magnitude. Higher surface areas result in more rapid simulated decreases in surface area. The surface area of siderite additionally decreases even more rapidly upon depletion of calcite. Unlike calcite, the surface area evolution of siderite varies among simulations where the two highest surface areas (BET specific surface areas, Fig. 8b, blue lines) approach a surface area of 0 around 40

hours, indicating siderite depletion. In the other simulations, it takes longer for the siderite surface area to decrease to 0 and siderite to be consumed. As can be expected from equation 3, the overall surface area evolutions are similar to volume fraction evolutions (Fig. 2a).

3.3.2 Long term surface area evolution

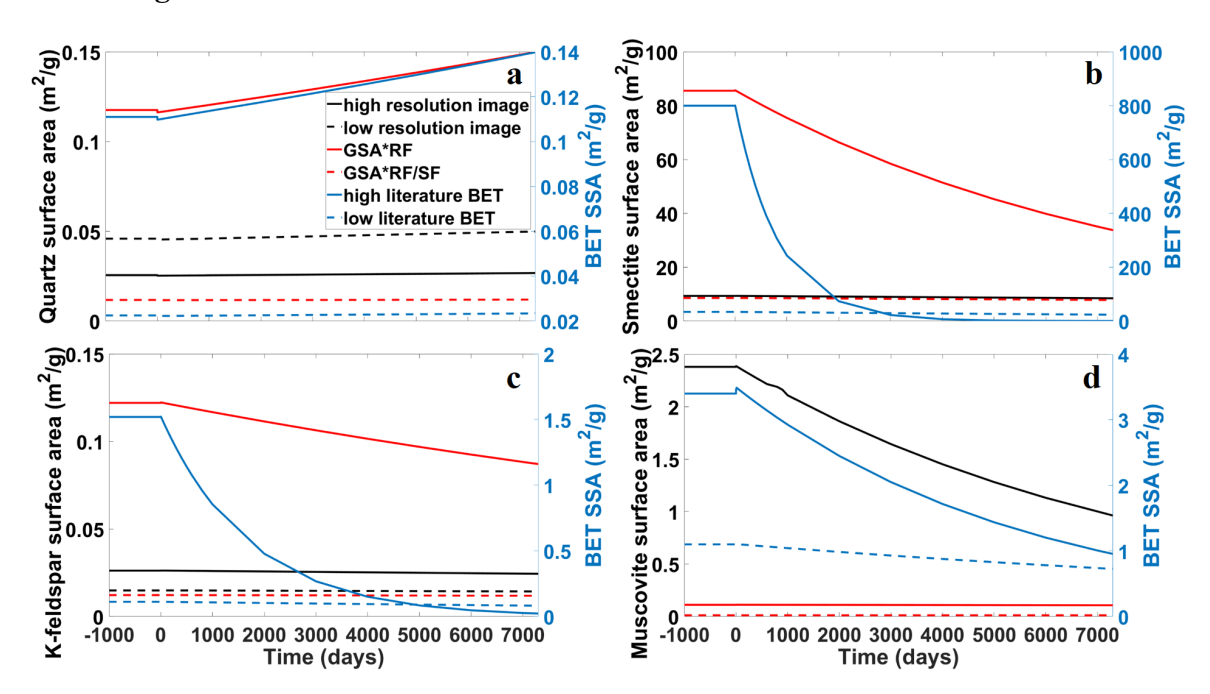


Fig. 9. Simulated mineral surface area evolution of non-carbonate minerals over 7300 days: (a) quartz, (b) smectite, (c) K-feldspar and (d) muscovite. The evolution of BET specific surface areas (blue lines) are plotted on the right y-axis.

The evolution of surface area for the non-carbonate minerals at longer times are shown in Fig.9. Some distinct variations in the simulated evolution of surface areas can be observed here. Little variation in the simulated evolution of surface area occurs in simulations using smaller surface area values. Conversely, increases and decreases in surface area occur in simulations using larger surface area values (blue and red lines in Fig. 9a, b and c, blue and black lines in Fig. 9d). Such changes also correspond to the volume fraction evolution in Fig. 5, where dissolution corresponds to a simulated decrease in the surface areas of the dissolving phases and precipitation to an increase in surface area. For example, in Fig. 9a, the surface area of quartz (SiO₂) increases as

SiO₂ precipitates (Fig. 5b, d, f, h).

4. Discussion

Table 4. Differences of the surface area values used in reactive transport simulations as compared to values obtained from the $0.34 \mu m$ images (high resolution). Surface area value differences = surface area value/surface area from high-resolution imaging.

	Surface area value differences					
Mineral	high resolution imaging	low resolution imaging	GSA _{RF} = GSA*RF	$\begin{array}{c} GSA_{SF} = \\ GSA_{RF}/SF \end{array}$	high BET literature	low BET literature
Quartz	1.00E+0	1.79E+0	4.61E+0	4.61E-1	4.34E+0	8.79E-1
K-feldspar	1.00E+0	5.69E-1	4.66E+0	4.66E-1	5.80E+1	4.27E+0
Calcite	1.00E+0	7.08E-1	1.05E+1	1.05E+0	1.49E+2	1.26E+0
Smectite	1.00E+0	1.00E+0	9.17E+0	9.17E-1	8.57E+1	3.64E+0
Muscovite	1.00E+0	1.00E+0	4.66E-2	4.66E-3	1.43E+0	4.62E-1
Siderite	1.00E+0	9.72E-1	4.46E+0	4.46E-1	2.92E+3	1.51E+2

Differences among the surface area values determined from images, calculated using geometric approaches, and collected from the literature are shown in Table 4 and vary by many orders of magnitude. In general, mineral accessible surface areas calculated from image analyses are small compared to specific surface area values obtained from BET analysis and geometric approaches. The differences between accessible surface areas calculated from images (0.34 µm and 5.71 µm resolutions) are within one order of magnitude. The differences between accessible surface areas and geometric surface areas are mostly within 1 order of magnitude, except for muscovite where there is more than 2 orders of magnitude variation. This, however, is largely dependent on the choice of roughness and scaling factor. Typically, a roughness factor of 10 and scaling factor one to three orders of magnitude is used (Peters, 2009; Landrot et al., 2012; Beckingham et al., 2016; Kweon and Deo, 2017), but there is little guidance in terms of how to select appropriate values. Specific surface areas measured using the BET approach are as much as 1-4 orders of magnitude higher than image obtained surface areas.

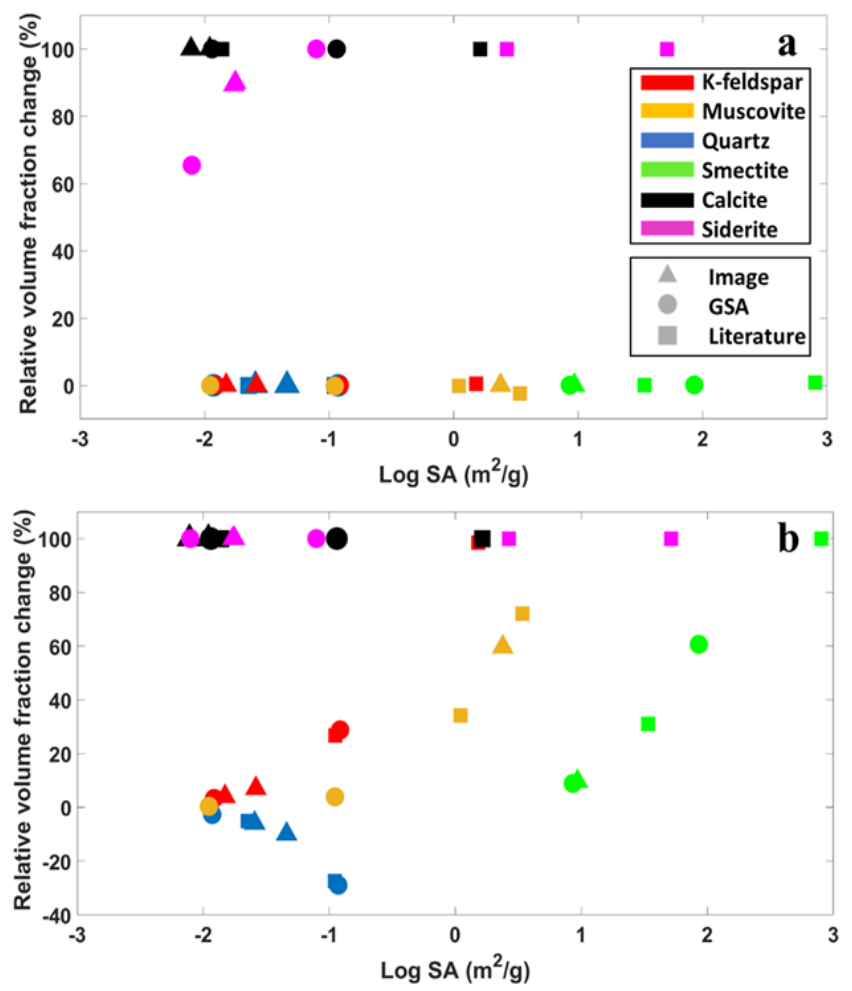


Fig. 10. Relative percentage change of simulated mineral volume fractions for different initial surface area values at (a) 170 hours and (b) 7300 days. Relative percentage change is the difference in the initial volume fraction and the final volume fraction over the initial volume fraction. Positive values indicate dissolution (decrease in volume fraction) and negative values indicate precipitation (increase in volume fraction). Simulations using image obtained surface areas are shown with triangles, geometric surface areas simulations with circles, and simulations using BET values from the literature shown with squares.

Mineral reaction rate directly increases with increasing mineral reactive surface area (e.g. Equation 1). This, however, results in different variations in mineral volume fractions among the different mineral phases. The simulated relative percentage change in mineral volume fractions with respect to the reactive surface area values used in the simulations for the different mineral phases is shown in Fig. 10. This reflects the total change in mineral volume fraction for 170 hours and 7300 days where complete dissolution is indicated by 100%.

Among all simulations, the surface area values of calcite vary up to 2 orders of

magnitude (Fig. 10). Such variations in calcite surface area resulted in no discernable differences in the evolution of calcite volume fraction at 170 hours or 7300 days, where these times correspond to typical laboratory or field conditions, for example. As such, simulations with different calcite surface areas, all reach calcite depletion around the same time (~35 hours). It can thus be inferred that if the timescale of interest in the simulation is beyond the timescale of calcite depletion, even larger variations in surface area will likely not yield any difference in the final simulated calcite volume fraction and contribution of calcite dissolution to porosity. The rate controlling process of the reaction needs to also be considered where reactions have been observed to be either surface or transport controlled. At the conditions considered, calcite has a high reaction rate constant and is very under-saturated in the solution such that the dissolution of calcite here is most likely transport-controlled rather than surface-controlled (Raines and Dewers, 1997; Morse and Arvidson, 2002; Morse et al., 2007). Pokrovsky et al. (2019) also observed that at elevated temperatures (60-100 °C) and pH < 4.5, the calcite reaction rate is not proportional to H⁺ activity at the mineral surface, but rather is controlled by transport of H⁺ to the calcite surface.

Siderite surface area values used here vary up to 4 orders of magnitude and variations in siderite volume fraction with changing surface area are quite obvious at 170 hours but no longer apparent at 7300 days (Fig. 10). In simulations using image obtained surface areas, siderite volume fractions change by 90% at 170 days. With one order of magnitude variation in geometric surface areas (Fig. 10a, magenta circles), the volume fraction of siderite changed by 65% and 100%, respectively. The two highest surface areas - BET specific surface areas, also result in complete consumption of siderite and a 100% decrease in siderite volume fraction at 170 hours. As all simulations result in complete siderite consumption within hundreds of hours, there is agreement in the overall change in siderite volume fraction at 7300 days, even though surface areas span 4 orders of magnitude.

Compared to calcite and siderite, the other four mineral phases have lower reaction rates. Large variations in surface areas for these phases result in less than 0.1% variation in volume fractions at 170 hours. Therefore, selecting surface areas for these mineral

phases from different sources would not have large effects on the simulated results if the goal was to understand the extent of reaction of these phases at shorter time scales, e.g. 170 hours or similar timescales. However, at longer times, the changes in mineral volume fraction can vary widely. As shown in Fig. 10, the differences of surface areas used in the six simulation scenarios are more than 2 orders of magnitude for K-feldspar and muscovite, around 2 orders of magnitude for smectite, and around 1 order of magnitude for quartz. Smaller K-feldspar surface areas result in minor (<5%) dissolution while K-feldspar is almost completely consumed (>95%) at 7300 days when larger surface areas are used. When BET specific surface areas are used (Fig. 8b, red square boxes), one order of magnitude variation in surface area results in significant differences in the evolution of mineral volume fractions (from 27% to 99%). On the other hand, when imaging-based accessible surface areas and geometric surface areas are used (Fig. 8b, red triangles and red circles), the resulted variations in mineral volume fractions are smaller (from 4% to 29%). A similar phenomenon occurs for muscovite where minor (<5%) dissolution of muscovite occurs when using lower values of surface area and 34% to 72% dissolution of muscovite occurs in simulations using higher surface areas at 7300 days. These variations in mineral volume fraction, however, require >2 orders of magnitude difference in surface area values. The extent of smectite dissolution also depends on surface area where the extent of dissolution increases with increasing surface area (8.9% to >99%). Small variations (<1 order of magnitude) in smectite surface area yield significant differences in the simulated volume fraction. This may lead to variations in estimated formation properties as clay minerals can largely alter the permeability and geomechanical properties of the formations, as observed for formations targeted for CO₂ injection (Bourg, 2015; Bourg et al., 2017).

611

612

613

614

615

616

617

618

619

620

621

622

623

624

625

626

627

628

629

630

631

632

633

634

635

636

637

638

639

640

Quartz surface areas vary by approximately one order of magnitude where increased precipitation occurs with increasing surface area. While the overall variation in volume fraction at the end of the simulation is smaller compared with other mineral phases, there is a significant impact on the resulting porosity because quartz is the most abundant mineral phase in the system (57.46%). As such, a difference in simulated

volume fraction of 10% to 30% results in significant variations in simulated sample porosity. Potential precipitation of additional mineral phases was also considered but no such phenomena is simulated to occur, most likely due to constant flow of CO₂-saturated brine and the corresponding consistent low pH conditions.

It should also be noted that while variations in surface areas may not result in discernable differences in mineral volume fractions (Fig. 5e and g), it can result in differences in the evolution of ion concentrations (Fig. 6e and g), which could lead to other changes the system. For instance, higher concentrations of magnesium and aluminum could promote precipitation of clay minerals downstream. The simulation model in this work considers CO₂-saturated brine constantly flowing through the system, maintaining pH at a low level – 3.5. This could represent the close-to-well zones during CO₂ injection, for example, where brine is saturated with CO₂. These conditions do not favor precipitation of carbonate or clay minerals but do correspond to conditions favorable for released SiO₂(aq) to precipitate as quartz. Variations in the simulated rate and extent of mineral dissolution and precipitation reactions in these systems could potentially lead to very different results, including changes in porosity and permeability critical for assessing the fate and impact of injected CO₂.

Mineral surface area evolution mimics the evolution of mineral volume fractions where higher initial surface areas result in faster reaction rates and faster changes in surface area (Equations 2 and 3). For minerals with higher reaction rates (e.g. calcite and siderite), the variations in the initial surface area have small impacts on the overall surface area evolution. For reactions with lower reaction rates that are more limited by reaction kinetics, variations in the initial surface area result in different evolutions of mineral surface area as well as mineral volume fraction. Minerals with lower reaction rates only have distinct changes in surface area at longer times, where variations in initial surface areas result in large differences in the evolution of mineral surface area (Fig. 9) as well as volume fraction (Fig. 5). For these minerals, higher initial surface areas result in simulated distinct changes over 7300 days, whereas lower surface areas remain stable throughout the 7300-day simulations (Fig. 9). For low reaction rate constants (e.g. non-carbonate minerals), impacts of variations surface area will be

lessened as reaction kinetics already limit the rate of reaction. However, in the higher ranges of surface area for these phases, where surfaces vary up to 4 orders of magnitude, variations in reaction kinetics are magnified.

Conclusions

This work aims to understand the impact of mineral surface area on simulated mineral reaction extents and reaction rates. Here, mineral surface areas values were obtained from image analyses, literature BET measurements and geometric approximations and used in reactive transport models to simulate CO₂-brine-mineral reactions under reservoir conditions over varying times. Six sets of surface area values were collected, two sets of accessible surface area calculated from image analyses, two sets of specific surface areas from BET measurements in the literature and specific and effective surface areas calculated using geometric approaches. Differences in these surface area values are several orders of magnitude. Variations in simulated results were observed but depend on the mineral phase as well as the time scale.

The variations in accessible surface area caused by image resolution differences are fairly small (< 1 order of magnitude) and have little impact on the simulated reactions on both short (hours) and long (years) time scales. However, selecting surface area values from the literature or calculating surface areas based on geometry could yield significantly different results in regard to the rate and extent of reactions as well as the long-term evolution of porosity.

Table 5. Summary of surface area impact on simulated mineral reactions and reaction rates in short term and long term. Numbers listed under surface area variations are referring to the surface area differences in orders of magnitude. Rate constant values: quartz (Brady and Walther, 1990), K-feldspar (Van Hees et al., 2002), calcite (Alkattan et al., 1998), smectite (Amram and Ganor, 2005), muscovite (Knauss and Wolery, 1988; Oelkers et al., 2008), siderite (Golubev et al., 2009).

Reactivity	Category	Mineral	Log k	Surface area variations in orders of magnitude	Short term	Long term
More reactive	carbonate	calcite	-4.21	1-2	minimum	minimum
		siderite	-5.69	1-4	large in higher SA range	minimum
More stable	non-clay	K-feldspar	-11.65	1-2	minimum	large in higher SA range
		muscovite	-12.67	1-3	minimum	large in higher SA range
		quartz	-11.60	1	minimum	large
	clay	smectite	-13.35	2	minimum	large

The extent of impact of variations in surface area on simulated mineral reactions and reaction rates depends on the time scale of interest. A summary of the observations varying surface areas had for each mineral phase over short and long time scales is given in Table 5. For minerals with fast reaction rates, large discrepancies in the simulated evolution of mineral phases will occur over short times (10s of hours) with varying surface areas. Among the more reactive minerals, calcite dissolution is not largely impacted by surface area variations while such impacts are more obvious for siderite. The overall impact of variations in calcite and siderite surface areas on the long-term evolution of the system (100s of hours), however, is small. For more stable minerals with lower reaction rates, such as K-feldspar, muscovite, smectite and quartz, variations in surface area have little impact on short time scales. Variations in reaction rates however are important over long times where large variations in the evolution of mineral volume fractions occur with different surface areas for these phases. Simulations also revealed that it is essential to have a good understanding of the quartz

surface area as the overall porosity evolution of the system is largely impacted by simulated SiO₂ precipitation.

714

715

716

717

718

719

720

721

722

723

724

725

726

727

728

729

730

731

732

733

734

735

736

737

738

739

740

741

742

743

Previous work found that accessible surface areas obtained from imaging better reflect the reactive surface areas and better reproduce the observed mineral reaction rates in core-flood experiments when comparing to other means of estimating reactive surface areas (Beckingham et al., 2017). Therefore, estimating accessible surface areas from imaging is generally preferred. However, imaging rock samples and then processing the 2D and 3D images to quantify accessible mineral surface areas is challenging and time and resource intensive. Higher resolution images are preferred when clay minerals are abundant (Qin and Beckingham, 2019), but this results in increased computational costs. Images with lower resolutions and proper processing can yield good results (mineral abundance, accessible surface area) and give similar simulated mineral reactions and reaction rates, especially in comparison to simulations carried out using surface areas calculated from higher resolution images. Depending on the purpose of the simulation, image analyses might not be necessary in some cases. For example, when simulating short term (10s of hours) CO₂-brine-mineral reactions with samples composed predominantly of more stable phases such as K-feldspar, using surface area calculated from images, BET values from the literature, or surface areas estimated from geometry yield similar results. This is also true for long term simulations (100s of hours) of CO₂-brine-mineral reactions for samples predominantly composed of highly reactive phases such as calcite. In either of these cases, imaging samples and processing captured images may not be necessary as other means of mineral surface area estimates are much less time and resource intensive and yield comparable results. However, when research interests are on the short-term evolution of samples composed of highly reactive phases (e.g. calcite and siderite) or the longterm evolution of samples composed of more stable phases (e.g. K-feldspar, muscovite, quartz, etc.), surface areas estimated using different approaches will largely impact the simulated results including the rate and extent of the reactions as well as the evolution of porosity. In these cases, a more thorough understanding of accessible mineral surface area is needed. Close attention also needs to paid to the surface area of precipitating

phases that may largely impact porosity, SiO₂ here, where differences in quartz surface area resulted in critical variations in porosity on long time scales. It was also observed here that other means of estimating effective surface area may be effective where simulations carried out using geometric effective surface areas that account for both surface roughness and surface site reactivity a agree relatively well with imaging-based simulations. However, this means of estimating surface area is largely imprecise and relies heavily on the choice of roughness and scaling factor, for which there is little guidance.

Acknowledgement

- 754 This work supported by the "Establishing an Early CO₂ Storage Complex in Kemper,
- 755 MS" project funded by the U.S. Department of Energy's National Energy Technology
- Laboratory and cost-sharing partners under grant number FE0029465, managed by the
- 757 Southern States Energy Board. Analysis of surface area evolution supported by the
- National Science Foundation under Grant No. EAR-1847243.

References

- 1. Aagaard, P. and Helgeson, H.C., 1982. Thermodynamic and kinetic constraints on reaction rates among minerals and aqueous solutions; I, Theoretical considerations. *American journal of Science*, 282(3), pp.237-285.
 - 2. Alemu, B.L., Aagaard, P., Munz, I.A. and Skurtveit, E., 2011. Caprock interaction with CO₂: A laboratory study of reactivity of shale with supercritical CO₂ and brine. *Applied Geochemistry*, 26(12), pp.1975-1989.
 - 3. Alkattan, M., Oelkers, E.H., Dandurand, J.L. and Schott, J., 1998. An experimental study of calcite and limestone dissolution rates as a function of pH from -1 to 3 and temperature from 25 to 80 C. *Chemical geology*, *151*(1-4), pp.199-214.
- 4. Altree-Williams, A., Brugger, J., Pring, A. and Bedrikovetsky, P., 2019. Coupled reactive flow and dissolution with changing reactive surface and porosity. *Chemical Engineering Science*, 206, pp.289-304.
- 5. Amram, K. and Ganor, J., 2005. The combined effect of pH and temperature on smectite dissolution rate under acidic conditions. *Geochimica et Cosmochimica Acta*, 69(10), pp.2535-2546.
- 6. Anbeek, C., 1992. Surface roughness of minerals and implications for dissolution studies. *Geochimica et Cosmochimica Acta*, 56(4), pp.1461-1469.
- 7. Apul, D.S., Gardner, K.H. and Eighmy, T.T., 2007. Modeling hydrology and

- reactive transport in roads: The effect of cracks, the edge, and contaminant properties. *Waste management*, *27*(10), pp.1465-1475.
- 8. Aradóttir, E.S.P., Sonnenthal, E.L., Björnsson, G. and Jónsson, H., 2012. Multidimensional reactive transport modeling of CO₂ mineral sequestration in basalts at the Hellisheidi geothermal field, Iceland. *International Journal of Greenhouse Gas Control*, 9, pp.24-40.

788

789

790

791 792

793

794 795

796

797

798 799

800 801

802

803 804

805 806

807

- 9. Audigane, P., Gaus, I., Czernichowski-Lauriol, I., Pruess, K. and Xu, T., 2007. Two-dimensional reactive transport modeling of CO₂ injection in a saline aquifer at the Sleipner site, North Sea. *American journal of science*, 307(7), pp.974-1008.
 - 10. Bachu, S., 2000. Sequestration of CO₂ in geological media: criteria and approach for site selection in response to climate change. *Energy conversion and Management*, 41(9), pp.953-970.
 - 11. Bacon, D.H., Sass, B.M., Bhargava, M., Sminchak, J. and Gupta, N., 2009. Reactive transport modeling of CO₂ and SO₂ injection into deep saline formations and their effect on the hydraulic properties of host rocks. *Energy Procedia*, *I*(1), pp.3283-3290.
 - 12. Beckingham, L.E., Mitnick, E.H., Steefel, C.I., Zhang, S., Voltolini, M., Swift, A.M., Yang, L., Cole, D.R., Sheets, J.M., Ajo-Franklin, J.B. and DePaolo, D.J., 2016. Evaluation of mineral reactive surface area estimates for prediction of reactivity of a multi-mineral sediment. *Geochimica et Cosmochimica Acta*, *188*, pp.310-329.
 - 13. Beckingham, L.E., Steefel, C.I., Swift, A.M., Voltolini, M., Yang, L., Anovitz, L.M., Sheets, J.M., Cole, D.R., Kneafsey, T.J., Mitnick, E.H. and Zhang, S., 2017. Evaluation of accessible mineral surface areas for improved prediction of mineral reaction rates in porous media. *Geochimica et Cosmochimica Acta*, 205, pp.31-49.
- 14. Black, J.R., Carroll, S.A. and Haese, R.R., 2015. Rates of mineral dissolution under CO₂ storage conditions. *Chemical Geology*, 399, pp.134-144.
- 15. Boano, F., Harvey, J.W., Marion, A., Packman, A.I., Revelli, R., Ridolfi, L. and Wörman, A., 2014. Hyporheic flow and transport processes: Mechanisms, models, and biogeochemical implications. *Reviews of Geophysics*, *52*(4), pp.603-679.
- 16. Bourg, I.C., 2015. Sealing shales versus brittle shales: a sharp threshold in the material properties and energy technology uses of fine-grained sedimentary rocks. *Environmental Science & Technology Letters*, 2(10), pp.255-259.
- 17. Bourg, I.C. and Ajo-Franklin, J.B., 2017. Clay, water, and salt: controls on the permeability of fine-grained sedimentary rocks. *Accounts of chemical research*, *50*(9), pp.2067-2074.
- 18. Bourg, I.C., Beckingham, L.E. and DePaolo, D.J., 2015. The nanoscale basis of CO₂ trapping for geologic storage. *Environmental science & technology*, 49(17), pp.10265-10284.
- 19. Brady, P.V. and Walther, J.V., 1989. Controls on silicate dissolution rates in neutral and basic pH solutions at 25 C. *Geochimica et Cosmochimica*

824 acta, 53(11), pp.2823-2830.

833

839

840

841

842 843

844 845

846

847 848

849

850 851

852

853

854 855

861

- 20. Brady, P.V. and Walther, J.V., 1990. Kinetics of guartz dissolution at low 825 826 temperatures. Chemical geology, 82, pp.253-264.
- 827 21. Brunauer, S., Emmett, P.H. and Teller, E., 1938. Adsorption of gases in 828 multimolecular layers. Journal of the American chemical society, 60(2), 829 pp.309-319.
- 22. Busenberg, E. and Clemency, C.V., 1976. The dissolution kinetics of feldspars 830 831 at 25 C and 1 atm CO₂ partial pressure. Geochimica et Cosmochimica Acta, 40(1), pp.41-49. 832
- 23. Caseri, W.R., Shelden, R.A. and Suter, U.W., 1992. Preparation of muscovite 834 with ultrahigh specific surface area by chemical cleavage. Colloid and Polymer Science, 270(4), pp.392-398. 835
- 24. Crandell, L.E., Ellis, B.R. and Peters, C.A., 2009. Dissolution potential of SO2 836 co-injected with CO₂ in geologic sequestration. Environmental science & 837 technology, 44(1), pp.349-355. 838
 - 25. Connell, L., Down, D., Lu, M., Hay, D. and Heryanto, D., 2015. An investigation into the integrity of wellbore cement in CO2 storage wells: Core flooding experiments and simulations. International journal of greenhouse gas control, 37, pp.424-440.
 - 26. Cubillas, P., Köhler, S., Prieto, M., Chaïrat, C. and Oelkers, E.H., 2005. Experimental determination of the dissolution rates of calcite, aragonite, and bivalves. Chemical Geology, 216(1-2), pp.59-77.
 - 27. Deng, S., Zuo, L., Aydin, A., Dvorkin, J. and Mukerji, T., 2015. Permeability characterization of natural compaction bands using core flooding experiments and three-dimensional image-based analysis: Comparing and contrasting the results from two different methods. AAPG Bulletin, 99(1), pp.27-49.
 - 28. Duan, Z. and Sun, R., 2003. An improved model calculating CO₂ solubility in pure water and aqueous NaCl solutions from 273 to 533 K and from 0 to 2000 bar. Chemical geology, 193(3-4), pp.257-271.
 - 29. Elkady, Y. and Kovscek, A.R., 2020. Multiscale study of CO2 impact on fluid transport and carbonate dissolution in Utica and Eagle Ford shale. Journal of Petroleum Science and Engineering, p.107867.
- 30. Erdem, M. and Özverdi, A., 2005. Lead adsorption from aqueous solution onto 856 siderite. Separation and Purification Technology, 42(3), pp.259-264. 857
- 858 31. Essaid, H.I., Bekins, B.A. and Cozzarelli, I.M., 2015. Organic contaminant 859 transport and fate in the subsurface: Evolution of knowledge and understanding. Water Resources Research, 51(7), pp.4861-4902. 860
- 32. Gautier, J.M., Oelkers, E.H. and Schott, J., 1994. Experimental study of Kfeldspar dissolution rates as a function of chemical affinity at 150 C and pH 862 9. Geochimica et Cosmochimica Acta, 58(21), pp.4549-4560.
- 864 33. Golubev, S.V., Bénézeth, P., Schott, J., Dandurand, J.L. and Castillo, A., 2009. Siderite dissolution kinetics in acidic aqueous solutions from 25 to 100 C and 0 865 to 50 atm pCO2. *Chemical Geology*, 265(1-2), pp.13-19. 866
- 34. Gouze, P. and Luquot, L., 2011. X-ray microtomography characterization of 867

- porosity, permeability and reactive surface changes during dissolution. *Journal* of contaminant hydrology, 120, pp.45-55.
- 35. Guo, B., Ma, L. and Tchelepi, H.A., 2018. Image-based micro-continuum model for gas flow in organic-rich shale rock. *Advances in Water Resources*, *122*, pp.70-84.
- 36. Grandclerc, A., Dangla, P., Gueguen-Minerbe, M. and Chaussadent, T., 2018. Modelling of the sulfuric acid attack on different types of cementitious materials. *Cement and Concrete Research*, 105, pp.126-133.

877878

882 883

884

885

886

892

893

894

895 896

897

- 37. Gunter, W.D., Perkins, E.H. and Hutcheon, I., 2000. Aquifer disposal of acid gases: modelling of water–rock reactions for trapping of acid wastes. *Applied geochemistry*, 15(8), pp.1085-1095.
- 38. Hellevang, H., Pham, V.T. and Aagaard, P., 2013. Kinetic modelling of CO₂– water–rock interactions. *International Journal of Greenhouse Gas Control*, *15*, pp.3-15.
 - 39. la Cecilia, D., Riley, W.J. and Maggi, F., 2019. Biochemical modeling of microbial memory effects and catabolite repression on soil organic carbon compounds. *Soil Biology and Biochemistry*, *128*, pp.1-12.
 - 40. Kennedy, M.J., Pevear, D.R. and Hill, R.J., 2002. Mineral surface control of organic carbon in black shale. *Science*, *295*(5555), pp.657-660.
- 41. Knauss, K.G., 1989. Muscovite dissolution kinetics as a function of pH and time at 70 C. *Geochimica et Cosmochimica Acta*, *53*(7), pp.1493-1501.
- 42. Knauss, K.G. and Wolery, T.J., 1988. The dissolution kinetics of quartz as a function of pH and time at 70 C. *Geochimica et Cosmochimica Acta*, *52*(1), pp.43-53.
 - 43. Kweon, H. and Deo, M., 2017. The impact of reactive surface area on brine-rock-carbon dioxide reactions in CO₂ sequestration. *Fuel*, *188*, pp.39-49.
 - 44. Landrot, G., Ajo-Franklin, J.B., Yang, L., Cabrini, S. and Steefel, C.I., 2012. Measurement of accessible reactive surface area in a sandstone, with application to CO₂ mineralization. *Chemical Geology*, 318, pp.113-125.
 - 45. Lasaga, A.C., 1981. Transition state theory. Rev. Mineral.; (United States), 8.
 - 46. Lasaga, A.C., 1984. Chemical kinetics of water-rock interactions. *Journal of geophysical research: solid earth*, 89(B6), pp.4009-4025.
- 47. Li, L., Maher, K., Navarre-Sitchler, A., Druhan, J., Meile, C., Lawrence, C.,
 Moore, J., Perdrial, J., Sullivan, P., Thompson, A. and Jin, L., 2017. Expanding
 the role of reactive transport models in critical zone processes. *Earth-science reviews*, 165, pp.280-301.
- 48. Liu, P., Zhang, T. and Sun, S., 2019. A tutorial review of reactive transport modeling and risk assessment for geologic CO2 sequestration. *Computers & geosciences*.
- 49. Maher, K. and Navarre-Sitchler, A., 2019. Reactive transport processes that drive chemical weathering: From making space for water to dismantling continents. *Reviews in Mineralogy and Geochemistry*, 85(1), pp.349-380.
- 50. Martens, E., Zhang, H., Prommer, H., Greskowiak, J., Jeffrey, M. and Roberts, P., 2012. In situ recovery of gold: Column leaching experiments and reactive

912 transport modeling. *Hydrometallurgy*, *125*, pp.16-23.

934

935 936

937

938 939

940

941

942 943

- 51. Martinez, B.C., DeJong, J.T. and Ginn, T.R., 2014. Bio-geochemical reactive transport modeling of microbial induced calcite precipitation to predict the treatment of sand in one-dimensional flow. *Computers and Geotechnics*, 58, pp.1-13.
- 52. Meakin, P. and Tartakovsky, A.M., 2009. Modeling and simulation of pore-scale multiphase fluid flow and reactive transport in fractured and porous media. *Reviews of Geophysics*, 47(3).
- 53. Metz, V., Raanan, H., Pieper, H., Bosbach, D. and Ganor, J., 2005. Towards the establishment of a reliable proxy for the reactive surface area of smectite. Geochimica et Cosmochimica Acta, 69(10), pp.2581-2591.
- 54. Miao, X., Wang, Y., Zhang, L., Wei, N. and Li, X., 2019. Improved Vinegar & Wellington calibration for estimation of fluid saturation and porosity from CT images for a core flooding test under geologic carbon storage conditions. *Micron*, 124, p.102703.
- 55. Morse, J.W. and Arvidson, R.S., 2002. The dissolution kinetics of major sedimentary carbonate minerals. *Earth-Science Reviews*, 58(1-2), pp.51-84.
- 56. Morse, J.W., Arvidson, R.S. and Lüttge, A., 2007. Calcium carbonate formation and dissolution. *Chemical reviews*, *107*(2), pp.342-381.
- 57. Navarre-Sitchler, A., Steefel, C.I., Sak, P.B. and Brantley, S.L., 2011. A reactivetransport model for weathering rind formation on basalt. *Geochimica et Cosmochimica Acta*, 75(23), pp.7644-7667.
 - 58. Navarre-Sitchler, A. and Jung, H., 2017. Complex Coupling of Fluid Transport and Geochemical Reaction Rates: Insights from Reactive Transport Models. *Procedia Earth and Planetary Science*, 17, pp.5-8.
 - 59. Ng, G.H.C., Bekins, B.A., Cozzarelli, I.M., Baedecker, M.J., Bennett, P.C., Amos, R.T. and Herkelrath, W.N., 2015. Reactive transport modeling of geochemical controls on secondary water quality impacts at a crude oil spill site near Bemidji, MN. *Water Resources Research*, *51*(6), pp.4156-4183.
 - 60. Nogues, J.P., Fitts, J.P., Celia, M.A. and Peters, C.A., 2013. Permeability evolution due to dissolution and precipitation of carbonates using reactive transport modeling in pore networks. *Water Resources Research*, 49(9), pp.6006-6021.
- 61. Noiriel, C., Luquot, L., Madé, B., Raimbault, L., Gouze, P. and Van Der Lee, J., 2009. Changes in reactive surface area during limestone dissolution: An experimental and modelling study. *Chemical Geology*, 265(1-2), pp.160-170.
- 62. Oelkers, E.H., Schott, J., Gauthier, J.M. and Herrero-Roncal, T., 2008. An experimental study of the dissolution mechanism and rates of muscovite. *Geochimica et Cosmochimica Acta*, 72(20), pp.4948-4961.
- 63. Pallud, C., Meile, C., Laverman, A.M., Abell, J. and Van Cappellen, P., 2007.
 The use of flow-through sediment reactors in biogeochemical kinetics:
 methodology and examples of applications. *Marine Chemistry*, 106(1-2),
 pp.256-271.
- 955 64. Papadopoulos, P. and Rowell, D.L., 1988. The reactions of cadmium with

calcium carbonate surfaces. *Journal of Soil Science*, *39*(1), pp.23-36.

- 65. Peters, C.A., 2009. Accessibilities of reactive minerals in consolidated sedimentary rock: An imaging study of three sandstones. *Chemical Geology*, 265(1-2), pp.198-208.
- 66. Pham, V.T.H., Lu, P., Aagaard, P., Zhu, C. and Hellevang, H., 2011. On the potential of CO₂-water-rock interactions for CO₂ storage using a modified kinetic model. *International Journal of Greenhouse Gas Control*, *5*(4), pp.1002-1015.
 - 67. Pokrovsky, O.S., Golubev, S.V., Schott, J. and Castillo, A., 2009. Calcite, dolomite and magnesite dissolution kinetics in aqueous solutions at acid to circumneutral pH, 25 to 150 C and 1 to 55 atm pCO2: New constraints on CO2 sequestration in sedimentary basins. *Chemical geology*, 265(1-2), pp.20-32.
 - 68. Qajar, J., 2012. Reactive Flow in Carbonate Cores via Digital Core Analysis.
 - 69. Qajar, J. and Arns, C.H., 2016. Characterization of reactive flow-induced evolution of carbonate rocks using digital core analysis-part 1: Assessment of pore-scale mineral dissolution and deposition. *Journal of contaminant hydrology*, 192, pp.60-86.
 - 70. Qin, F. and Beckingham, L.E., 2019. Impact of image resolution on quantification of mineral abundances and accessible surface areas. *Chemical Geology*, 523, pp.31-41.
 - 71. Raines, M. and Dewers, T., 1997. "Mixed" kinetics control of fluid-rock interaction in reservoir production scenarios. *Journal of Petroleum Science and Engineering*, 17(1-2), pp.139-155.
 - 72. Salehikhoo, F., Li, L. and Brantley, S.L., 2013. Magnesite dissolution rates at different spatial scales: The role of mineral spatial distribution and flow velocity. *Geochimica et Cosmochimica Acta*, 108, pp.91-106.
 - 73. Scheibe, T.D., Mahadevan, R., Fang, Y., Garg, S., Long, P.E. and Lovley, D.R., 2009. Coupling a genome-scale metabolic model with a reactive transport model to describe in situ uranium bioremediation. *Microbial biotechnology*, *2*(*2*), pp.274-286.
 - 74. Schmidt, M.J., Pankavich, S.D., Navarre-Sitchler, A. and Benson, D.A., 2019. A Lagrangian method for reactive transport with solid/aqueous chemical phase interaction. *Journal of Computational Physics: X, 2*, p.100021.
- 75. Schmidt, M.J., Pankavich, S.D., Navarre-Sitchler, A., Engdahl, N.B., Bolster, D. and Benson, D.A., 2019. Reactive Particle-tracking Solutions to a Benchmark Problem on Heavy Metal Cycling in Lake Sediments. 2019arXiv190809818S.
- 76. Sen, T.K. and Khilar, K.C., 2006. Review on subsurface colloids and colloidassociated contaminant transport in saturated porous media. *Advances in colloid* and interface science, 119(2-3), pp.71-96.
- 77. Shan, Y. and Guo, H., 2013. Fluoride adsorption on modified natural siderite: Optimization and performance. *Chemical engineering journal*, *223*, pp.183-191.
- 78. Shultz, C.D., Bailey, R.T., Gates, T.K., Heesemann, B.E. and Morway, E.D., 2018. Simulating selenium and nitrogen fate and transport in coupled stream-aquifer systems of irrigated regions. *Journal of Hydrology*, 560, pp.512-529.

79. Steefel, C.I., Appelo, C.A.J., Arora, B., Jacques, D., Kalbacher, T., Kolditz, O., Lagneau, V., Lichtner, P.C., Mayer, K.U., Meeussen, J.C.L. and Molins, S., 2015. Reactive transport codes for subsurface environmental simulation. *Computational Geosciences*, 19(3), pp.445-478.

1004

1005

1006

10071008

1009

1012

1013

1014

10151016

1017

10201021

1022

10231024

10251026

1027

10281029

1030

1031

- 80. Steefel, C.I., DePaolo, D.J. and Lichtner, P.C., 2005. Reactive transport modeling: An essential tool and a new research approach for the Earth sciences. *Earth and Planetary Science Letters*, 240(3-4), pp.539-558.
 - 81. Steefel, C.I., Molins, S. and Trebotich, D., 2013. Pore scale processes associated with subsurface CO2 injection and sequestration. *Reviews in Mineralogy and Geochemistry*, 77(1), pp.259-303.
- 82. Steefel, C., 2018. Reactive Transport Modeling: Applications in Subsurface Energy and Environmental Problems. John Wiley & Sons.
 - 83. Tester, J.W., Worley, W.G., Robinson, B.A., Grigsby, C.O. and Feerer, J.L., 1994. Correlating quartz dissolution kinetics in pure water from 25 to 625 C. *Geochimica et Cosmochimica Acta*, *58*(11), pp.2407-2420.
 - 84. Van Hees, P.A.W., Lundström, U.S. and Mörth, C.M., 2002. Dissolution of microcline and labradorite in a forest O horizon extract: the effect of naturally occurring organic acids. *Chemical Geology*, 189(3-4), pp.199-211.
- 1018 85. White, A.F. and Peterson, M.L., 1990. Role of reactive-surface-area characterization in geochemical kinetic models.
 - 86. White, S.P., Allis, R.G., Moore, J., Chidsey, T., Morgan, C., Gwynn, W. and Adams, M., 2005. Simulation of reactive transport of injected CO₂ on the Colorado Plateau, Utah, USA. *Chemical geology*, 217(3-4), pp.387-405.
 - 87. Xu, T., Kharaka, Y.K., Doughty, C., Freifeld, B.M. and Daley, T.M., 2010. Reactive transport modeling to study changes in water chemistry induced by CO₂ injection at the Frio-I Brine Pilot. *Chemical Geology*, 271(3-4), pp.153-164.
 - 88. Yabusaki, S.B., Fang, Y., Williams, K.H., Murray, C.J., Ward, A.L., Dayvault, R.D., Waichler, S.R., Newcomer, D.R., Spane, F.A. and Long, P.E., 2011. Variably saturated flow and multicomponent biogeochemical reactive transport modeling of a uranium bioremediation field experiment. *Journal of contaminant hydrology*, 126(3-4), pp.271-290.
- 89. Yang, Y., Bruns, S., Stipp, S.L.S. and Sørensen, H.O., 2018. Impact of microstructure evolution on the difference between geometric and reactive surface areas in natural chalk. *Advances in water resources*, 115, pp.151-159.